IEEE Access
Multidisciplinary | Rapid Review | Open Access Journal

Received July 29, 2020, accepted August 14, 2020, date of publication August 19, 2020, date of current version August 31, 2020.

Digital Object Identifier 10.1109/ACCESS.2020.3017788

Rotor Stress and Dynamics Analysis of a High-Speed Permanent Magnet Machine for a Micro Gas Turbine Considering Multiphysics Factors

MENGZI ZHENG, WEIGUANG HUANG, AND CHUANG GAO
Shanghai Advanced Research Institute, Chinese Academy of Sciences, Shanghai 201210, China
School of Chemical Engineering, University of Chinese Academy of Sciences, Beijing 100049, China

Corresponding author: Chuang Gao (gaoc@sari.ac.cn)

This work was supported by the Innovation Academy of Light-duty Gas Turbine and the Key Programs of Chinese Academy of Sciences under Project ZDRW-CN-2017-2.

ABSTRACT For high-speed permanent magnet machines (HSPMMs), the precise analysis of rotor stress and rotor dynamics is essential to ensure the stable operation of rotor under high-speed conditions. This work conducts an in-depth research on the rotor of an HSPMM for a micro gas turbine with predetermined geometrical sizes. Firstly, the mechanical and electromagnetic losses are investigated by both, empirical methods and finite element method (FEM) respectively, and then the 3D steady-state temperature distribution of the HSPMM is evaluated on this basis. Then, considering the non-isothermal temperature field of the rotor, the 3D thermal-structural coupling method is adopted to analyze the influence of the carbon fiber wrapping direction and the epoxy resin adhesive between permanent magnets (PMs) and rotor core on the rotor thermal stress. Furthermore, in the steady-state thermal field, considering the change in elastic modulus and the generation of thermal stress caused by temperature rise, the results of the modal analysis are compared with those of room temperature to analyze the effect of temperature on the natural frequency of the rotor. Finally, two prototypes of 80 kW, 60000 rpm HSPMMs are fabricated to test the capability of the HSPMM. The experimental results of back-to-back drag test and modal test verify the accuracy of the temperature characteristics and modal analysis, respectively.

INDEX TERMS Coupling analysis, high-speed permanent magnet machines, rotor dynamics, thermal stress.

I. INTRODUCTION

High-speed permanent magnet machines (HSPMMs) have been gaining popularities in academics and industrial applications, such as gas turbines, distributed power generation systems, gas compression appliances, and spindle drives, due to their advantages of high-power density, high efficiency, and direct drive [1], [2]. For micro gas turbines, the HSPMMs can be directly connected to the high-speed rotor, eliminating the traditional gearbox, thus reducing its volume and noise, while increasing its efficiency, reliability, and stability. From the design point of view, HSPMMs have various challenges that need to be addressed, including power loss, temperature field, rotor thermal stress, and rotor dynamics, which are also the key factors in the design of HSPMMs [3]. Because of the low tensile strength and operating temperature of permanent magnets (PMs), the ultimate output power of HSPMMs is mostly subject to the mechanical and thermal constraints of the PMs [4], [5]. To ensure the reliability of high-speed rotor operation, the high strength, low density carbon fiber sleeve (CFS) is usually adopted to protect the PMs. However, the low thermal conductivity of carbon fiber hampers the heat dissipation of the PMs, which will lead to irreversible demagnetization of PMs [6], [7]. Therefore, reducing power loss and efficient heat dissipation are the direct ways to solve this problem [8]. Furthermore, in order to avoid operating on the bending critical speed, it is essential to precisely predict the rotor dynamics of the rotor-bearing system. Therefore, the successful design and operation of HSPMMs require simultaneous consideration of the multiphysics factors already mentioned [9], [10].

The power loss and thermal analysis of HSPMMs were investigated quite intensively in recent years. Liu *et al.* [11] proposed an improved model of HSPMM iron loss

The associate editor coordinating the review of this manuscript and approving it for publication was Wei Xu.

considering multiphysics factors. The errors between model calculations and measured values were less than 5%. Du *et al.* [12] used the measured current waveform as excitation for the time-stepping finite element method (FEM) to gain the exact rotor eddy current loss. Wrobel *et al.* [13] developed a method to deduce the AC winding loss based on temperature variation. Air friction loss is obtained by analytical methods [14]–[16], though considering the complex fluid flow characteristics, the air friction loss was investigated through computational fluid dynamics (CFD) as in [17]. The bearing losses can be estimated by empirical approaches [18]–[20].

This paper mainly focuses on the research of thermal stress distribution and rotor dynamics of the carbon fiber wrapped PM rotor. For the rotor thermal stress analysis, previous studies have paid the most attention to the influence of centrifugal force, interference fit, and temperature gradient on the rotor stress. The previous studies used the simplified model ignoring the wrapping direction of the CFS and the influence of epoxy resin adhesive (ERA) between the PMs and rotor core [21]–[25]. Additionally, the micro gas turbine rotor, especially the turbine wheel, operates at very high temperatures. The significant increase in rotor temperature causes greater thermal stress in the rotor assembly and notable changes in material properties, such as the elastic modulus. These combined factors affect the rotor stiffness, thus changing the natural frequency [26], [27]. However, few researches can be found about the thermal-structure-rotor dynamics coupling theory of HSPMMs till now, and the influence of temperature on rotor dynamics has been neglected in previous studies [8], [14], [20], [28].

Herein, an 80 kW, 60000 rpm HSPMM for a micro gas turbine is taken as the research object. The rotor stress and dynamics are further studied under the consideration of multiphysics constraints, such as power loss, thermal field and mechanical strength. In order to explore the rotor thermal stress distribution in more detail, the influences of the wrapping direction of the CFS and the ERA between the PMs and the rotor core on the rotor stress distribution are considered. Moreover, in order to predict the natural frequencies of the rotor system more accurately, the thermal-structure-rotor dynamics coupling research is also studied. The accuracy of the calculations is verified by comparison with experimental data.

II. POWER LOSS AND THERMAL ANALYSIS

The main parameters of the HSPMM are listed in Table 1. In summary, the HSPMM has a 4-pole radial magnetized PM rotor and a 24-slot stator in the form of distributed windings. A CFS is used for improving rotor strength. The stator core is formed by laminating 0.1 mm thick low-iron power-consuming electrical steel sheets. An oil jacket encompasses the rotor outer surface to remove heat from the HSPMM. Different bearing types are used at each end of the rotor. The front bearing is a tilting pad bearing, which only supports radial loads. The rear bearing is a four-point bearing, which is a kind of ball bearing, and supports both radial and axial loads. The centrifugal compressor and turbine are back-to-back and overhung. The cross-section view and radial view of the HSPMM are displayed in Figure 1 and Figure 2, respectively.

TABLE 1. Main parameters of the HSPMM.

Parameter	Value
Rated power (kW)	80
Rated speed (rpm)	60000
Rated frequency (Hz)	2000
Rated current (A)	60
Pole number	4
Slot number	24
Permanent magnet	SmCo
Retaining sleeve	Carbon fiber

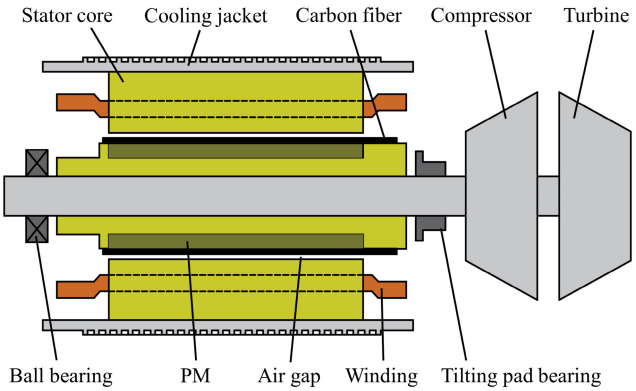

FIGURE 1. Cross-section view of the HSPMM.

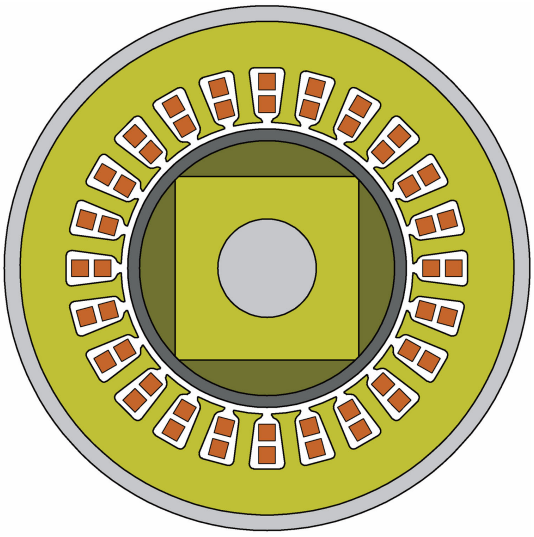

FIGURE 2. Radial view of the HSPMM.

A. POWER LOSS ANALYSIS

The power loss analysis is a key step in the HSPMMs analysis. Due to the limited volume, the loss distribution must be

accurately calculated to ensure that the cooling system can provide sufficient heat dissipation and the stable operation of the machine.

According to the empirical method proposed by Palmgren in [18], the power loss of a four-point bearing can be estimated from the bearing friction moment as

$$P_{bearing} = 10^3 M_{total}\omega \tag{1}$$

where ω is the angular speed, M_{total} is the total friction moment, which is composed of the viscous and load-related friction moments. The total friction moment can be obtained by adding the various moment parts as [18]

$$M_{total} = M_0 + M_1 \tag{2}$$

where M_0 is the viscous friction moment, M_1 is the load-related friction moment. The viscous part can be predicted as [18]

$$M_0 = 10^{-7} f_0 (nv)^{2/3} D_a^3 \tag{3}$$

where f_0 is a value related to the bearing and lubrication type. For four-point bearings, when oil lubrication is used, the value of f_0 is 4. Values can be obtained in the literature [19]. n is the bearing speed, v is the operating viscosity, and D_a is the average diameter of the inner and outer diameters of the bearing, that is, the pitch circle. The load-related part can be predicted as

$$M_1 = f_1 F_a D_a^3 \tag{4}$$

where f_1 is an index taking into account the load. For our four-point bearing, the value can be estimated as 0.0003 [19]. F_a is the average load applied to the bearings.

For the tilting pad bearing, the temperature of the lubricating oil in the bearing can be predicted to be 86 ° by measuring the oil temperature of the lubricating oil flowing out of the bearing, which can be used as the thermal boundary for a steady-state thermal analysis.

Due to high speed rotation, the air friction loss generated within the clearance in HSPMMs becomes significant and should not be ignored. This loss can be estimated using the following analytical method [16]:

$$P_f = \frac{1}{32} K_f C_f \pi \rho \omega^3 D_r^4 L_a \tag{5}$$

where K_f is the roughness factor, the value of smooth surface is 1.0, the value of axial grooved surface is 2.5 [29], C_f is the air friction coefficient that depends on the diameter of the rotor, the radial air-gap length δ, and the Reynolds number Re_δ, ρ is the air density, D_r is the rotor diameter, and L_a is the active length of the stator-rotor assembly, respectively.

The air friction coefficient within the different flow regimes is calculated according to the measurements in [30]

$$\begin{cases} C_f = 0.515 \dfrac{(2\delta/D_r)^{0.3}}{Re_\delta^{0.5}}, (500 < Re < 10^4) \\ C_f = 0.0325 \dfrac{(2\delta/D_r)^{0.3}}{Re_\delta^{0.2}}, (Re > 10^4) \end{cases} \tag{6}$$

The properties of the tangential airflow in the air gap can be described by the Couette-Reynolds number [30]:

$$Re_\delta = \frac{\rho \omega D_r \delta}{2\mu} \tag{7}$$

where μ is the air dynamic viscosity. Herein, the roughness factor of the smooth surface is taken as 1.0, the air density is 1.29 kg · m^{-3}, and the air dynamic viscosity is 1.79×10^{-5} Pa · s.

For this HSPMM, there is no axial forced air cooling in the air gap, so the losses caused by axial air flow and Taylor vortices can be neglected.

The iron, rotor eddy-current, and copper losses are calculated by FEM. The calculation results of the loss distribution of the HSPMM under the rated operating condition are shown in Table 2.

TABLE 2. Power loss distribution.

Power loss component	Value (W)
Iron loss	432
Rotor eddy current loss	67
Copper loss	352
Air friction loss	353
Four-point bearing loss	586
Total loss	1790

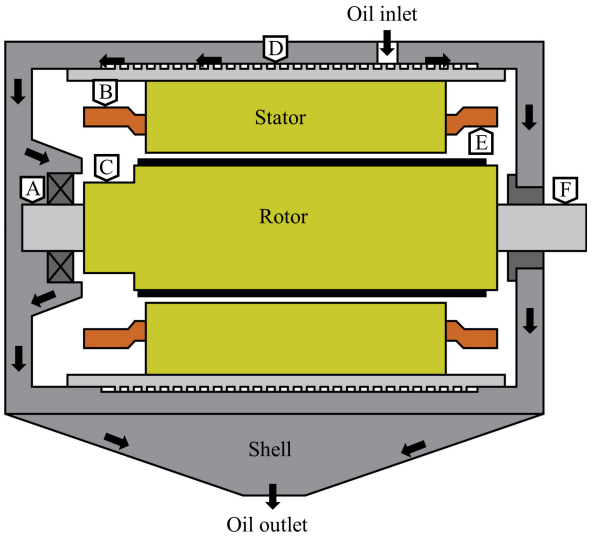

FIGURE 3. Oil system and the positions of HTCs.

B. THERMAL ANALYSIS

The HSPMM is cooled by lubricating oil, and the oil is also used to cool and lubricate the bearings at both ends of the machine, as shown in Figure 3. The steady-state thermal analysis is performed by using 3D FEM. The calculation of the temperature field depends largely on the properties of the materials as shown in Table 3. The iron, rotor eddy current, copper, air friction and bearing losses are applied to the thermal model in the form of heat generated inside

TABLE 3. Material properties of the HSPMM.

Material	Density (kg/m^3)	Thermal conductivity (W/m/°C)	Specific heat capacity (J/kg/°C)
Stator core	7490	20	496
Sleeve	1600	1	800
PM	8400	12	350
Rotor core	7850	46	582
Shaft	7780	17	502
Compressor	7780	19	502
Turbine	8500	12	380
Winding	7850	380	400

TABLE 4. Thermal boundary conditions.

Position		HTC ($W/m^2/°C$)
A	Shaft rear end	1000
B	Winding end	40
C	Rotor end	304
D	Cooling jacket	694
E	Winding end	214
F	Shaft front end	1000

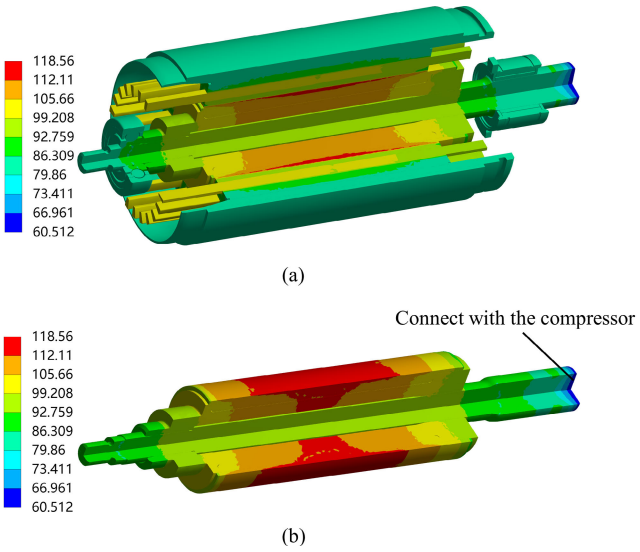

FIGURE 4. Temperature distribution of the HSPMM. (a) The whole temperature distribution. (b) The rotor temperature distribution (Unit: °).

the components. The heat transfer coefficients (HTCs) are the thermal boundary conditions of the thermal analysis. As shown in Figure 3, points A-F show the positions of the HTCs, and the values of the HTCs at each position are listed in Table 4.

The calculated temperature of the turbine is 800°C, which greatly exceeds the temperature inside the HSPMM. In order to better show the details of the internal temperature distribution of the HSPMM, the calculation results in Figure 4 hide the compressor and the turbine. It can be seen that due to the poor thermal conductivity of the CFS and the high-speed rotation of the rotor, the maximum temperature of 119°C occurs on the rotor surface, and the temperature of each component of the HSPMM is within the allowable range. It can also be obviously seen that the thermal field of the rotor is non-isothermal, and both radial and axial temperature gradients are clearly visible. The temperature at the position where the shaft is connected to the compressor is only 61°C, indicating that the high temperature of the turbine has little effect on the HSPMM temperature. Therefore, the results of the temperature calculation can be verified by the back-to-back towing test.

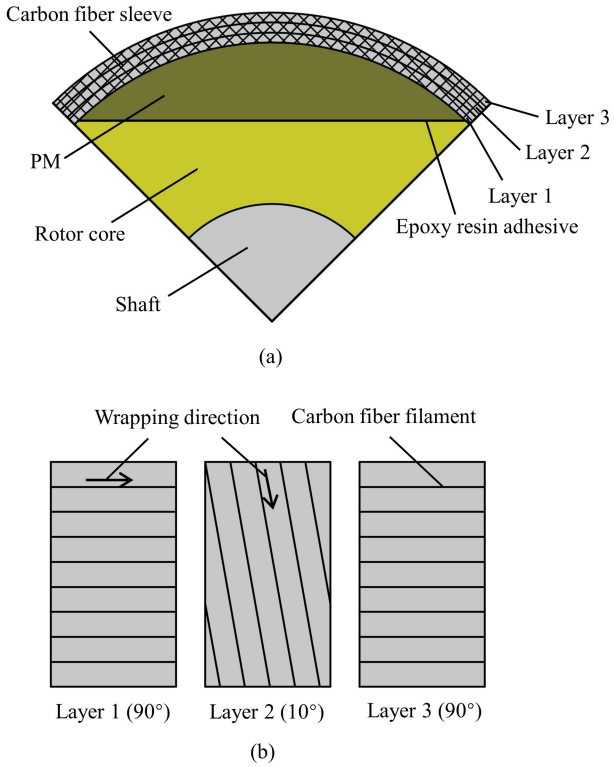

FIGURE 5. Geometric representation of the rotor. (a) The rotor wrapped with multiple layers of carbon fiber. (b) The carbon fiber wrapping direction of model B and model C.

III. ROTOR THERMAL STRESS ANALYSIS

A. ROTOR GEOMETRY

The geometry of the HSPMM rotor is displayed in Figure 5. It has four main components: shaft, rotor core, PMs, and CFS. The PMs are glued to the outer surface of the rotor core by the ERA. In order to explore the rotor stress in more detail, the influence of the ERA cannot be ignored. The carbon fiber filament is wrapped on the outer surface of the PMs by large tension wrapping to form a specific pre-tightening force. Considering the wrapping process, the CFS is divided into three layers, and each layer has its own wrapping direction. The wrapping direction along the axial direction is defined as 0°, and the wrapping direction perpendicular to the axial direction is defined as 90°.

According to different circumstances, the CFS can be fabricated by different manufacturing processes. When making a prototype, wrapping carbon fiber filament directly around the

TABLE 5. Comparison of the three rotor models.

Rotor model	Wrapping direction of the layer 2	Whether to consider the ERA
Model A	90°	Yes
Model B	10°	Yes
Model C	10°	No

rotor is a relatively simple method. In case of mass production, the CFS should be made in advance, and the rotor will be inserted into it by interference assembly. At assembly time, the CFS will be subjected to a high axial force to overcome the interference fit, so the axial wrapping should be considered when designing the CFS. To obtain the suitable rotor solution for the HSPMM, three rotor schemes (model A, B, C, listed in Table 5) are compared. The wrapping directions of the layer 1 and layer 3 of the CFS in the three models are both 90°. The layer 2 of the CFS of model A is also 90°, which does not need to bear an axial force and is suitable for prototypes. Considering the angle limit of the carbon fiber wrapping equipment, the wrapping direction of the layer 2 of the CFS is set as 10° in model B, which enables the CFS to withstand a certain axial force and is suitable for mass production. The ERA is not considered in model C. Compare models B and C to study the effect of the ERA on rotor stress. Figure 5 (b) shows the wrapping directions of the CFS in models B and C.

B. THERMAL STRESS

The rotor of the HSPMM is mostly of a compound structure. Under the rated working condition, the rotor is heated and expanded. Due to the different coefficient of thermal expansion (CTE) and thermal conductivity among the rotor components, the temperature distribution of the rotor is not uniform. In the previous rotor thermal stress researches, the temperature was mostly set as a constant value, ignoring the temperature gradient along the radial and axial directions of the rotor, and thus the effect of the temperature gradient on the stress distribution was ignored. In this work, the calculation result of temperature field is imported into the stress field as a thermal load to calculate the rotor thermal stress distribution under the thermal-structural coupling. The interference between the PMs and the CFS is 0.2 mm, and the rated rotor speed is 60000 rpm. The material properties of the rotor components are listed in Table 6, and the rotor thermal stress analysis is performed accordingly. The failure of the CFS is judged by the Tsai-Wu stress criterion, which is the most famous and classic criterion for describing the damage of composite materials in the existing mature criteria, and other criteria can be simplified from the Tsai-Wu criterion based on specific load and stress conditions [31]. According to this criterion, the CFS with the Tsai-Wu coefficient greater than 1 is regarded as a failure [32].

The thermal stress distributions of the PM and the CFS of the three models are shown in Figure 6. The tensile strength of the PMs used in this HSPMM is 350 MPa,

TABLE 6. Material properties of the HSPMM.

Material property		Elastic modulus (GPa)	Poisson ratio	CTE (μm/m/℃)
Turbine		156	0.28	15
Compressor		196	0.3	11
Shaft		198	0.3	11
Rotor core		205	0.29	13
PM		100	0.28	8
CFS	Tangential	130	0.3	0
	Radial	10	0.3	3

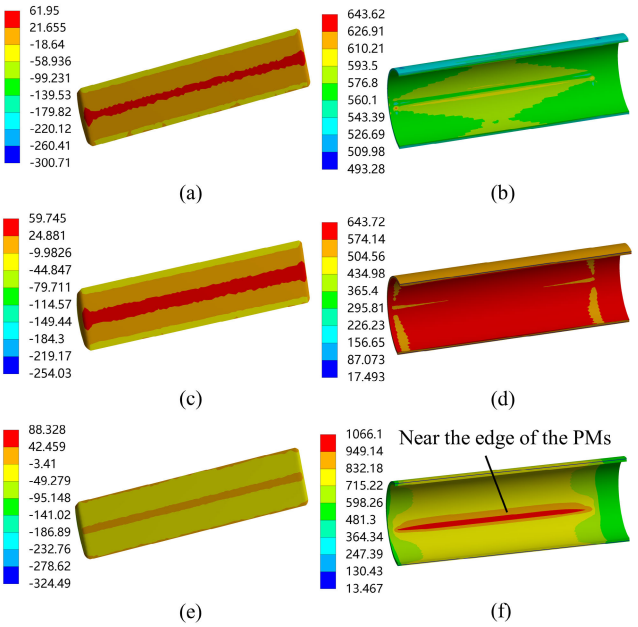

FIGURE 6. Rotor thermal stress of the three models. (a) PM radial stress of model A. (b) CFS tangential stress of model A. (c) PM radial stress of model B. (d) CFS tangential stress of model B. (e) PM radial stress of model C. (f) CFS tangential stress of model C (Unit: MPa).

and the compressive strength is 850 MPa. By comparing Figure 6(a) and (c), the area and the value of the compressive stress of the PMs in model A are larger than that of model B. It is calculated that the average radial tensile stress of the PMs in model A is 8 MPa, and that of the PMs in model B is 13 MPa, indicating that when the CFS wrapping direction of layer 2 is 90°, the PMs are in a better compression state, and the CFS can better withstand the centrifugal force generated by the PMs. In addition, it can be clearly seen that the force conditions of model A and model B can meet the requirements of safe operation for the HSPMM. As mentioned above, the model A can be used for prototype production, and the model B is more appropriate for mass production.

Figures 6 (c) and (e) show that the PMs in model C are in a better state of compression than in model B. This is due to the influence of the ERA between the PMs and the rotor core is considered within the model. The ERA can bear part of the centrifugal force produced by the PMs. The PMs bottom surface is affected by both tensile stress and

compressive stress, and when the ERA is not considered, the PM bottom surface is mainly affected by compressive stress from CFS. However, in this case, the CFS will bear most of the centrifugal force generated by the PMs, making the local stress of the CFS increase, as shown in Figure 6 (f).

It can be seen from Figures 6 (b) and (d) that the maximum stress of model A is close to that of model B, but the minimum stress of model A is much larger than that of model B, which is caused by the different wrapping directions of layer 2 of the CFS. When the wrapping direction of layer 2 is 90°, the force object of layer 2 is carbon fiber filament; when the wrapping direction of layer 2 is 10°, the force object of layer 2 is mainly the resin matrix. Figure 6 (f) shows that when the ERA is not considered, there will be stress concentration on the CFS near the edge of the PMs, and the Tsai-Wu coefficient at this position is greater than 1, indicating the failure of the CFS at this position, as shown in Figure 7. This is because the CFS needs to withstand most of the centrifugal force generated by the PMs and the deformation of the middle part of the CFS in contact with the PMs is greater than the deformation on both sides, resulting in bending. Therefore, it is necessary to select the ERA that can work stably under the rated working conditions of HSPMMs, thereby reducing the stress of the CFS.

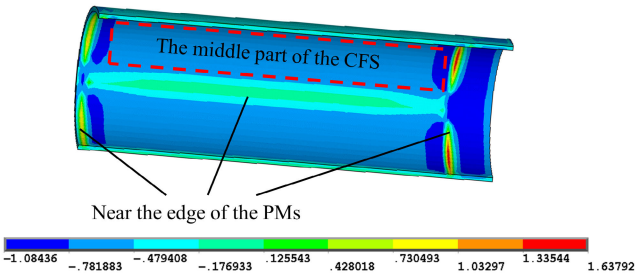

FIGURE 7. Tsai-Wu coefficient distribution of the model C.

IV. ROTOR DYNAMICS

The rotor of a micro gas turbine operates in a high-temperature environment, especially the turbine used for expanding high-temperature gas. The elastic modulus of the rotor materials change with temperature, and the temperature rise will cause the rotor thermal stress as calculated previously. These factors together affect the rotor stiffness, and thus the rotor natural frequency. However, the influence of temperature on rotor dynamics of HSPMMs has been ignored in previous studies, leading to some analysis results that are not sufficiently accurate. Next, this paper will focus on how temperature affects the natural frequency of the rotor.

As shown in Table 7, since the turbine operates in an extremely high-temperature environment, its elastic modulus is significantly lower than that at room temperature. In order to eliminate the influence of the supports, the rotor is modeled in a free-free support state. The first three natural frequencies of transverse vibration of the rotor are calculated by FEM at room temperature and rated steady-state temperature

TABLE 7. Temperature dependent elastic modulus.

Material property		Elastic modulus (GPa)	
		Room temperature	Steady-state temperature
Turbine		199	156
Compressor		206	196
Shaft		206	198
Rotor core		209	205
PM		108	100
CFS	Tangential	130	120
	Radial	10	9

TABLE 8. Comparison of the natural frequencies at room temperature and steady-state temperature.

Modes	Room temperature	Steady-state temperature	Difference
First bending (Hz)	375.08	346.22	8.3%
Second bending (Hz)	1604.9	1477.37	8.6%
Third bending (Hz)	3787.78	3494.26	8.4%

respectively, and the mode shapes of vibration under these two conditions are compared. The results indicate that the mode shapes at room temperature and steady-state temperature are basically the same, as expected and not shown here. However, the natural frequencies of the rotor are obviously different in these two cases. As summarized in Table 8, compared with the room temperature condition, the natural frequencies of the first three modes of the steady-state temperature field are decreased by at least 8.3%, which cannot be ignored for HSPMMs that are sensitive to speed, especially those used in gas turbines. Therefore, when the rotor of the HSPMM works in a high-temperature environment, the influence of temperature on the natural frequency needs to be considered to make the calculation more accurate.

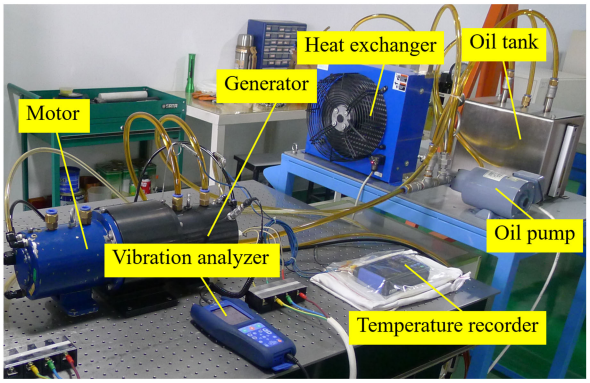

FIGURE 8. Temperature test rig.

V. EXPERIMENTAL VALIDATION

A. TEMPERATURE TEST

The accuracy of calculation needs to be verified by testing the hardware. Two identical prototypes are fabricated to test the capability of the HSPMM, and a test rig of back-to-back towing test is built, as shown in Figure 8. In this

experiment, one HSPMM serves as a motor to drive another HSPMM which serves as a generator, until the HSPMM is operating steadily at the rated speed 60000 rpm. In order to realize the back-to-back towing experiments, two shafts with internal and external splines were fabricated to enable the two HSPMMs to be connected back to back. Because of the complexity of spline connections between high speed shafts, a vibration analyzer is employed to monitor the vibration of the HSPMMs in real time.

An external oil cooling system with heat exchanger is used to provide oil maintained a steady low temperature. As shown in Figure 9, four thermistors installed at different positions of the HSPMM are used to measure the temperature values, and the figure also shows the simulation result of the HSPMM temperature field. The measurement results and calculation results under the rated condition are compared in Figure 10. The calculation results agree well with the measurement results, indicating the accuracy of the simulation method, which can be used for the subsequent thermal stress analysis and modal analysis.

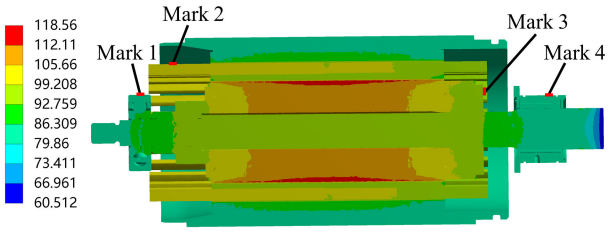

FIGURE 9. Temperature field and the locations of the thermistors embedded (Unit: °).

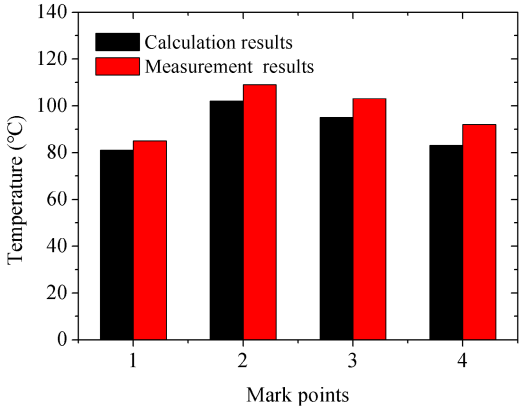

FIGURE 10. Comparison of the measurement and calculation results of temperature.

B. MODAL TEST

The calculation results of the natural frequencies under room temperature are verified with a rotor modal test. Figure 11 shows the modal test setup of the rotor. The free-free natural frequencies of the rotor are measured by using twelve acceleration sensors. The acceleration sensors are

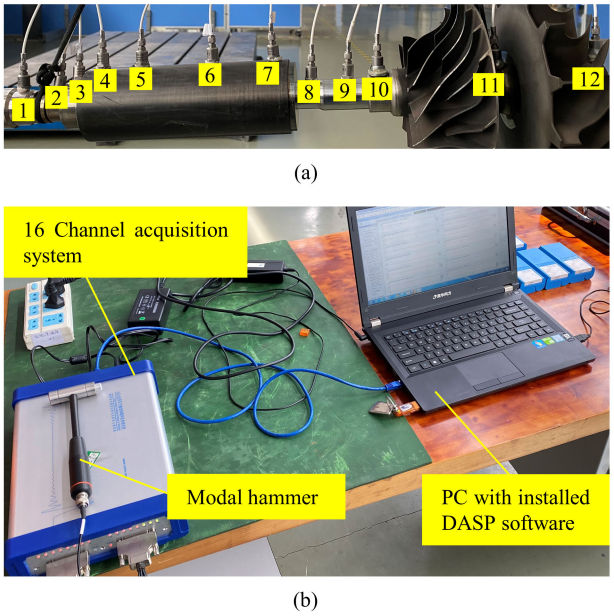

FIGURE 11. Modal test setup. (a) Sensors locations. (b) Acquisition system.

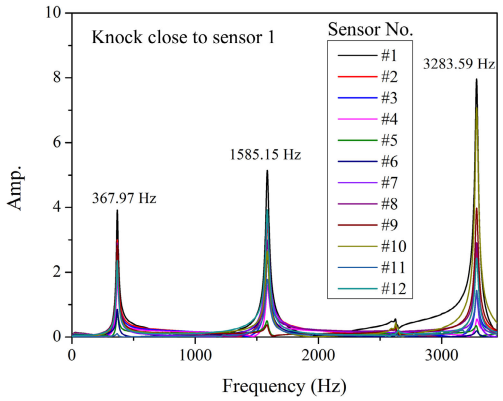

FIGURE 12. Frequency spectrum of the rotor.

fixed on the rotor surface, and the rotor is hanged to simulate the free-free boundary condition. The vibration amplitude is recorded by the acceleration sensors. Figure 12 shows the frequency spectrum of the rotor, which is obtained by the fast Fourier transform (FFT) of the output signal of each sensor after the rotor is struck by the modal hammer. In the experiment, the striking position is near sensor 1. The peaks of the first three bending natural frequencies can be clearly observed in the spectrum. The first bending natural frequency is 367.97 Hz, the second is 1585.15 Hz, and the third is 3283.59 Hz. Table 9 shows the comparison between the measured and calculated values. It can be seen that the calculation results are in good agreement with the measured values. The errors of the first three bending frequencies are 1.9%, 1.2%, and 1.5%, respectively. Therefore, the accuracy of the steady-state temperature field calculation and the accuracy of the modal calculation at room temperature can indirectly

TABLE 9. Comparison of the measurement and calculation values of natural frequencies at room temperature.

Modes	Calculation	Measurement	Error
First bending (Hz)	375.08	367.97	1.9%
Second bending (Hz)	1604.9	1585.15	1.2%
Third bending (Hz)	3787.78	3283.59	1.5%

demonstrate the correctness of the modal analysis at steady-state temperature.

VI. CONCLUSION

This paper has presented an 80 kW, 60000 rpm HSPMM for a micro gas turbine. The thermal stress of the rotor with different CFS schemes and the influence of temperature on the natural frequencies of the rotor are studied. The key conclusions are summarized as follows:

1) The CFS of the HSPMM is wrapped with three layers of carbon fiber. Compared with the CFS with the middle layer wrapping direction close to the axial direction (10°), the PMs are in better compression state when all three layers are circumferentially wrapped (90°), and the CFS can withstand the centrifugal force generated by the PMs to a greater extent. Therefore, when designing the CFS, a large proportion of 90° wrapping should be used. However, considering mass production, the CFS is required to withstand a certain axial force during assembly, so the axial laying of the carbon fiber needs to be considered. Therefore, two rotor models are proposed for prototype production (model A) and mass production (model B) respectively. The CFS of model A only considers the circumferential wrapping, and model B wrapping direction of the middle layer is closer to the axial direction. Both models can ensure the safe operation of the rotor.

2) In order to further analyze the stress state of the rotor at high speed, a comparative analysis of the two cases of excluding and considering the ERA between the PMs and the rotor core is carried out. When the effect of the ERA is not considered (the ERA can bear part of the centrifugal force generated by the PMs), the PMs are in a better compression state than when considering the ERA. However, the CFS needs to bear most of the centrifugal forces generated by the PMs, resulting in local stress concentrations, which may lead to local failures of the CFS. Therefore, it is a good practice to keep the ERA working at the operating condition to reduce the stress of the CFS.

3) The results of the modal analysis considering the temperature rise show that when the rotor is operated in a high-temperature environment, the influence of temperature on the natural frequency cannot be ignored. The temperature rise decreases the elastic modulus of the materials and generates thermal stress, both of which causes the drop of the natural frequencies of the HSPMM rotor by at least 8.3% compared to normal temperature. Therefore, for speed-sensitive equipment such as HSPMMs, especially those used in gas turbines, it is necessary to consider the influence of temperature on the rotor dynamics in the design and calculation, which leading more accurate prediction results.

ACKNOWLEDGEMENT

The authors would like to thank for the fruitful discussion and help by Dr. Wu Fuxian and Konstantin Shaposhnikov from Helan Turbines Company Ltd.

REFERENCES

[1] A. Tenconi, S. Vaschetto, and A. Vigliani, "Electrical machines for high-speed applications: Design considerations and tradeoffs," *IEEE Trans. Ind. Electron.*, vol. 61, no. 6, pp. 3022–3029, Jun. 2014.
[2] D. Gerada, A. Mebarki, N. L. Brown, C. Gerada, A. Cavagnino, and A. Boglietti, "High-speed electrical machines: Technologies, trends, and developments," *IEEE Trans. Ind. Electron.*, vol. 61, no. 6, pp. 2946–2959, Jun. 2014.
[3] F. R. Ismagilov, N. Uzhegov, V. E. Vavilov, V. I. Bekuzin, and V. V. Ayguzina, "Multidisciplinary design of ultra-high-speed electrical machines," *IEEE Trans. Energy Convers.*, vol. 33, no. 3, pp. 1203–1212, Sep. 2018.
[4] W. Li, H. Qiu, X. Zhang, J. Cao, S. Zhang, and R. Yi, "Influence of rotor-sleeve electromagnetic characteristics on high-speed permanent-magnet generator," *IEEE Trans. Ind. Electron.*, vol. 61, no. 6, pp. 3030–3037, Jun. 2014.
[5] A. Smirnov, N. Uzhegov, T. Sillanpää, J. Pyrhönen, and O. Pyrhönen, "High-speed electrical machine with active magnetic bearing system optimization," *IEEE Trans. Ind. Electron.*, vol. 64, no. 12, pp. 9876–9885, Dec. 2017.
[6] W. Li, X. Zhang, S. Cheng, and J. Cao, "Thermal optimization for a HSPMG used for distributed generation systems," *IEEE Trans. Ind. Electron.*, vol. 60, no. 2, pp. 474–482, Feb. 2013.
[7] N. Bianchi, S. Bolognani, and F. Luise, "Potentials and limits of high-speed PM motors," *IEEE Trans. Ind. Appl.*, vol. 40, no. 6, pp. 1570–1578, Nov./Dec. 2004.
[8] H. Fang, R. Qu, J. Li, P. Zheng, and X. Fan, "Rotor design for high-speed high-power permanent-magnet synchronous machines," *IEEE Trans. Ind. Appl.*, vol. 53, no. 4, pp. 3411–3419, Jul./Aug. 2017.
[9] S. Li, Y. Li, W. Choi, and B. Sarlioglu, "High-speed electric machines: Challenges and design considerations," *IEEE Trans. Transport. Electrific.*, vol. 2, no. 1, pp. 2–13, Mar. 2016.
[10] K. Reichert and G. Pasquarella, "High speed electric machines status trends and problems," in *Proc. IEEE/KTH Stockholm Tech. Conf.*, Stockholm, Sweden, Nov. 1995, pp. 41–49.
[11] G. Liu, M. Liu, Y. Zhang, H. Wang, and C. Gerada, "High-speed permanent magnet synchronous motor iron loss calculation method considering multiphysics factors," *IEEE Trans. Ind. Electron.*, vol. 67, no. 7, pp. 5360–5368, Jul. 2020.
[12] G. Du, W. Xu, J. Zhu, and N. Huang, "Power loss and thermal analysis for high-power high-speed permanent magnet machines," *IEEE Trans. Ind. Electron.*, vol. 67, no. 4, pp. 2722–2733, Apr. 2020.
[13] R. Wrobel, D. E. Salt, A. Griffo, N. Simpson, and P. H. Mellor, "Derivation and scaling of AC copper loss in thermal modeling of electrical machines," *IEEE Trans. Ind. Electron.*, vol. 61, no. 8, pp. 4412–4420, Aug. 2014.
[14] Z. Huang and J. Fang, "Multiphysics design and optimization of high-speed permanent-magnet electrical machines for air blower applications," *IEEE Trans. Ind. Electron.*, vol. 63, no. 5, pp. 2766–2774, May 2016.
[15] H. Fang, D. Li, R. Qu, J. Li, C. Wang, and B. Song, "Rotor design and eddy-current loss suppression for high-speed machines with a solid-PM rotor," *IEEE Trans. Ind. Appl.*, vol. 55, no. 1, pp. 448–457, Jan./Feb. 2019.
[16] J. E. Vrancik, "Prediction of windage power loss in alternators," NASA, Washington, DC, USA, Tech. Note TN D-4849, Oct. 1968, pp. 1–18.
[17] B. Dong, K. Wang, B. Han, and S. Zheng, "Thermal analysis and experimental validation of a 30 kW 60000 r/min high-speed permanent magnet motor with magnetic bearings," *IEEE Access*, vol. 7, pp. 92184–92192, Jul. 2019.
[18] A. Palmgren, *Ball and Roller Bearing Engineering*. Philadelphia, PA, USA: SKF Industries, 1959.
[19] J. Brändlein, P. Eschmann, L. Hasbargen, and K. Weigand, *Ball and Roller Bearings: Theory, Design and Application*. Chichester, U.K.: Wiley, 1999.

[20] N. Uzhegov, E. Kurvinen, J. Nerg, J. Pyrhonen, J. T. Sopanen, and S. Shirinskii, "Multidisciplinary design process of a 6-slot 2-pole high-speed permanent-magnet synchronous machine," *IEEE Trans. Ind. Electron.*, vol. 63, no. 2, pp. 784–795, Feb. 2016.
[21] A. Borisavljevic, H. Polinder, and J. A. Ferreira, "Enclosure design for a high-speed permanent magnet rotor," in *Proc. 5th IET Conf. PEMD*, Brighton, U.K., Apr. 2010, pp. 1–5.
[22] F. Zhang, G. Du, T. Wang, G. Liu, and W. Cao, "Rotor retaining sleeve design for a 1.12-MW high-speed PM machine," *IEEE Trans. Ind. Appl.*, vol. 51, no. 5, pp. 3675–3685, Sep./Oct. 2015.
[23] K. Grace, S. Galioto, K. Bodla, and A. M. El-Refaie, "Design and testing of a Carbon-Fiber-Wrapped synchronous reluctance traction motor," *IEEE Trans. Ind. Appl.*, vol. 54, no. 5, pp. 4207–4217, Sep./Oct. 2018.
[24] K. Yu, S. Yin, and X. Xie, "Design and analysis of high speed rotor in air-core pulsed alternator," *IEEE Access*, vol. 7, pp. 140367–140374, Sep. 2019.
[25] J.-H. Ahn, C. Han, C.-W. Kim, and J.-Y. Choi, "Rotor design of high-speed permanent magnet synchronous motors considering rotor magnet and sleeve materials," *IEEE Trans. Appl. Supercond.*, vol. 28, no. 3, pp. 1–4, Apr. 2018.
[26] M. Zhuo, L. Yang, and L. Yu, "The steady-state thermal effect on dynamic characteristics of gas turbine rotor considering contact effect," in *Proc. IEEE Int. Conf. Mechatronics Autom.*, Aug. 2014, pp. 981–986.
[27] L. Gu and F. Chu, "An analytical study of rotor dynamics coupled with thermal effect for a continuous rotor shaft," *J. Sound Vib.*, vol. 333, no. 17, pp. 4030–4050, Aug. 2014.
[28] Z. Huang and Y. Le, "Rotordynamics modelling and analysis of high-speed permanent magnet electrical machine rotors," *IET Electr. Power Appl.*, vol. 12, no. 8, pp. 1104–1109, Sep. 2018.
[29] Z. Huang, J. Fang, X. Liu, and B. Han, "Loss calculation and thermal analysis of rotors supported by active magnetic bearings for high-speed permanent-magnet electrical machines," *IEEE Trans. Ind. Electron.*, vol. 63, no. 4, pp. 2027–2035, Apr. 2016.
[30] E. Bilgen and R. Boulos, "Functional dependence of torque coefficient of coaxial cylinders on gap width and Reynolds numbers," *J. Fluids Eng.*, vol. 95, no. 1, pp. 122–126, Mar. 1973.
[31] S. W. Tsai and E. M. Wu, "A general theory of strength for anisotropic materials," *J. Composite Mater.*, vol. 5, no. 1, pp. 58–80, Jan. 1971.
[32] H. T. Hahn and S. W. Tsai, *Introduction to Composite Materials*. Westport, CT, USA: Technic Publishing, 1980.

MENGZI ZHENG received the B.S. degree in material engineering from Shenyang Ligong University, Shenyang, China, in 2013, and the M.S. degree in control engineering from Shanghai University, Shanghai, China, in 2018. He is currently pursuing the Ph.D. degree in chemical engineering with the Shanghai Advanced Research Institute, Chinese Academy of Sciences, Shanghai. Since 2013, he has been working with the Shanghai Advanced Research Institute, Chinese Academy of Sciences. His research interest includes the design and calculation of high-speed permanent-magnet machines.

WEIGUANG HUANG received the B.S. and Ph.D. degrees from the Department of Aeronautical Engineering, Kyushu University, Japan, in 1986 and 1991, respectively.

From 1998 to 2010, he served as the Deputy Director, the Executive Deputy Director, and the Director of the Institute of Engineering Thermophysics, Chinese Academy of Sciences, Shanghai, China. Since 2008, he has been the Director of the Center for Clean Energy Technology, Chinese Academy of Sciences, where he has been the Vice President of the Shanghai Advanced Research Institute since 2010. His research interests include numerical simulation and study mechanism of full 3D viscous flow, unsteady dynamic and static cascade interference, complex flow characteristics and loss mechanism in turbomachines, and high-speed rotating machines.

CHUANG GAO received the B.S. degree in mechanical engineering from the Jiangsu University of Science and Technology, Zhenjiang, China, in 2003, and the Ph.D. degree in fluid machinery from Shanghai Jiao Tong University, Shanghai, China, in 2010.

Since 2010, he has been an Associate Professor with the Shanghai Advanced Research Institute, Chinese Academy of Sciences, Shanghai. He has authored more than 20 articles and holds more than 15 inventions. His research interests include aerodynamics of radial turbomachinery, rotor dynamics, and high-speed generators.